

## Rescattering Processes for Elliptical Polarization: A Quantum Trajectory Analysis

R. Kopold, D. B. Milošević,\* and W. Becker†

*Max-Born-Institut, Max-Born-Strasse 2a, 12489 Berlin, Germany*

(Received 22 September 1999)

High-harmonic generation and high-order above-threshold ionization spectra calculated in the strong-field approximation are analyzed in terms of the complex space-time orbits that result from a saddle point analysis of the underlying integrals. For elliptical polarization, the plateaus of the spectra of high-harmonic generation and high-order above-threshold ionization each turn into a staircase of very similar appearance. Each step of the stair can be traced to a particular pair of orbits which are almost identical in both cases.

PACS numbers: 42.50.Hz, 31.15.Kb, 32.80.Rm, 42.65.Ky

When atoms are exposed to high-intensity laser fields characteristic effects become visible, whose general appearance is largely independent of the individual atomic species [1]. The examples that have been most extensively investigated are the generation of very high harmonics of the incident laser field and the production of very hot electrons. The spectra of both processes exhibit a plateau structure. There is general agreement that the physical origin of both phenomena is very similar: electrons that have been freed through tunneling and accelerated away from the ion by the laser field may be accelerated back to the ion so that they have the opportunity to recombine generating high harmonics, or to rescatter and subsequently acquire additional kinetic energy. These processes are dominated by the interaction of the electron with the laser field, which explains the universality of the plateau and its cutoff.

In the physical understanding of these processes for linear polarization, the concept of quantum paths has proved very fertile and has been applied extensively, in particular for high-harmonic generation (HHG) [2–4], but also for high-order above-threshold ionization (HATI) [5], that is, for the above mentioned very hot electrons. These quantum paths are complex electron trajectories in space and time. Their real parts largely agree with the orbits of the so-called simple-man model [6,7] (see also Refs. [8,9]) which describes the aforementioned rescattering scenario in completely classical terms, neglecting the binding potential. The quantum paths have, however, imaginary parts which are small for parameter values where the orbits are classically admissible. These imaginary parts are related to the quantum-mechanical origin of the electron through tunneling. The matrix element for HHG or HATI can be represented as the coherent sum of the exponentials of the action of these orbits, allowing for their constructive or destructive interference, as mandated by the quantum-mechanical path integral. The magnitude of the imaginary part of an orbit determines its weight in this sum via the ensuing imaginary part of the action. Indeed, in HHG experiments it was possible to identify the contributions of individual orbits via their different collective behavior [10].

The extension of the simple-man model to laser polarizations other than linear has met with difficulties: If the

electron starts with zero velocity it never returns to its origin. Owing to wave packet spreading, HHG and HATI may still occur [11,12] and have indeed been observed in experiments [13,14]. However, currently, there is no model that works for elliptical polarization and preserves the charm and predictive power of the simple-man model.

In this Letter, we present HATI and HHG spectra for an elliptically polarized monochromatic driving field calculated using an improved Keldysh approximation [15] that allows for one single act of rescattering, or the Lewenstein model [2], respectively, and we analyze these spectra in terms of quantum paths.

For the matrix element for ionization into a state with asymptotic momentum  $\mathbf{p}$  we use the approximation [15]

$$M_{\mathbf{p}} \sim \int_{-\infty}^{\infty} dt \int_{-\infty}^t dt' \langle \psi_{\mathbf{p}}(t) | V U(t, t') V | \psi_0(t') \rangle, \quad (1)$$

where  $\psi_{\mathbf{p}}(t)$  denotes the Volkov wave function with asymptotic momentum  $\mathbf{p}$ ,  $U(t, t')$  the Volkov propagator, and  $\psi_0(t)$  the initial bound state with binding energy  $E_0$ . The binding potential  $V$  in Eq. (1) is arbitrary. We will use a regularized zero-range potential which eliminates the spatial integrations. For HHG, we employ the Lewenstein model [2] which leads to an expression having the same structure as Eq. (1). Henceforth, results based on the numerical evaluation of either expression will be referred to as “exact.”

In order to proceed towards the interpretation of these “exact” results in terms of quantum paths we expand the Volkov propagator in terms of the Volkov wave functions. We are then left with the five-dimensional integral

$$M_{\mathbf{p}} \sim \int_{-\infty}^{\infty} dt \int_0^{\infty} d(t-t') \int d^3k \exp[iS(t, t', \mathbf{k})]. \quad (2)$$

For HATI, the approximated exponent is

$$S(t, t', \mathbf{k}) = -\frac{1}{2m} \int_t^{\infty} d\tau [\mathbf{p} - e\mathbf{A}(\tau)]^2 - \frac{1}{2m} \int_{t'}^t d\tau [\mathbf{k} - e\mathbf{A}(\tau)]^2 + \int_{-\infty}^{t'} d\tau |E_0|. \quad (3)$$

The two variables of integration  $t'$  and  $t$  in the form (2) can be interpreted as the start time and the return (rescattering or recombination) time of the simple-man model, and the three terms of the action (3) illustrate the various approximations made: a ground state unperturbed by the field for times earlier than  $t'$ , propagation in the laser field unperturbed by the binding potential for times in between the start time  $t'$  and the return time  $t$ , and final propagation in the laser field after rescattering.

Stationary points  $(t_S, t'_S, \mathbf{k}_S)$  of the action (3) are given by the solutions of the three equations [5]:

$$[\mathbf{k} - e\mathbf{A}(t')]^2 = -2m|E_0|, \quad (4)$$

$$[\mathbf{k} - e\mathbf{A}(t)]^2 = [\mathbf{p} - e\mathbf{A}(t)]^2, \quad (5)$$

$$(t - t')\mathbf{k} = \int_{t'}^t d\tau e\mathbf{A}(\tau). \quad (6)$$

Of these, the first expresses energy conservation when the electron at time  $t'$  tunnels into the continuum, the second enforces elastic rescattering at time  $t$ , and the third makes sure that the electron returns to its starting point. For HHG of a photon with frequency  $\Omega = n\omega$ , the only difference is that the right-hand side of Eq. (5) is replaced by  $2m(\Omega - |E_0|)$ .

The saddle point equations (4)–(6) contain the crucial differences between linear and elliptical polarization: for the former, owing to Eq. (6),  $\mathbf{k}$  is along the field. Hence, the initial velocity  $\mathbf{v}_0 \equiv [\mathbf{k} - e\mathbf{A}(t')]/m$  is purely imaginary in view of Eq. (4). In consequence,  $t'$ ,  $t$ , and  $\mathbf{k}$  acquire imaginary parts. If, however, the binding energy  $|E_0|$  is neglected, the initial velocity vanishes,  $t$ ,  $t'$ , and  $\mathbf{k}$  become real, and the standard simple-man model is recovered. In contrast, for elliptical polarization, we can no longer conclude that the initial velocity is a purely imaginary vector. Equation (4) states only that its real and imaginary part must be perpendicular.

In terms of the solutions  $(t_S, t'_S, \mathbf{k}_S)$  of the saddle point equations, the matrix element can be written as

$$M_{\mathbf{p}} \sim \sum_n \left[ \det \left( \frac{\partial^2 S}{\partial q_j \partial q_k} \right) \right]^{-1/2} \exp[iS(t_{S_n}, t'_{S_n}, \mathbf{k}_{S_n})], \quad (7)$$

where  $q_j (j, k = 1, \dots, 5)$  runs over the five variables  $t_S, t'_S$ , and  $\mathbf{k}_S$ . The quantum paths contributing to the sum have to be judiciously identified.

As an overview, we display in Fig. 1 ATI spectra for various ellipticities, calculated from Eq. (1). The most noticeable feature is the dramatic drop of the yields of the rescattered electrons as soon as the ellipticity exceeds  $\xi \sim 0.1$ . At the same time, the cutoff rather slowly recedes to lower energies. Actually, for sufficiently high ellipticity, there are several plateaus, each with its own cutoff. For example, for  $\xi = 0.5$ , Fig. 1 shows cutoffs at the electron energies  $E \sim 3U_p, 5U_p, 7U_p$ , and  $8.5U_p$ , each of which might determine the cutoff observed in an experiment, depending on the experimental sensitivity.

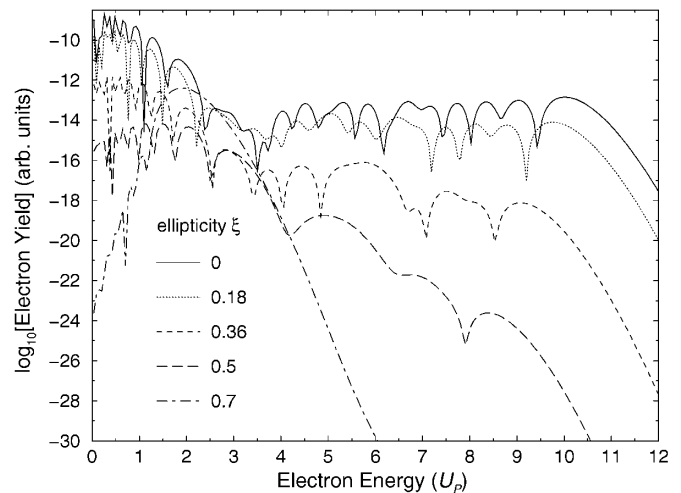


FIG. 1. ATI spectra in the direction of the large component of the field  $\mathbf{F}(t) = (F/\sqrt{1 + \xi^2})(\hat{\mathbf{x}} \sin \omega t - \xi \hat{\mathbf{y}} \cos \omega t)$  for various ellipticities  $\xi$  as indicated. The ponderomotive potential  $U_p = e^2 F^2 / (4m\omega^2)$  is kept constant while  $\xi$  varies. The parameters are  $\omega = 0.0584$  a.u. ( $\lambda = 782$  nm),  $U_p/\omega = 17.9$  ( $I = 5 \times 10^{14}$  W/cm $^2$ ), and  $E_0 = -0.9$  a.u. (helium). The highest cutoff for  $\xi = 0.7$  is outside of the figure with a yield of  $10^{-38}$  at  $E = 8.2U_p$ .

The main point of this Letter now is the comparison of the exact calculation with the approximate evaluation (7) which is based on the saddle point trajectories or quantum paths determined from the solutions of Eqs. (4)–(6). Figure 2 depicts successive approximations to the spectrum of Fig. 1 for  $\xi = 0.5$ . The dot-dashed curve represents the result of incorporating the two trajectories with the shortest travel time  $t - t'$ . They determine the exact spectrum just before the cutoff with the highest

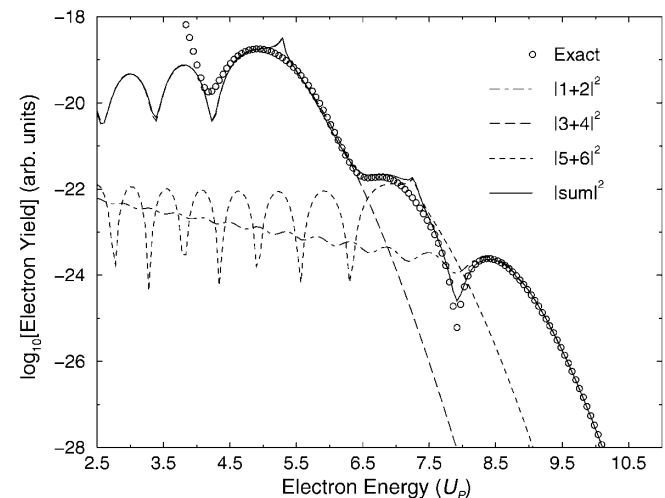


FIG. 2. The high-energy part of Fig. 1 for  $\xi = 0.5$ . The circles indicate the exact yields for the individual ATI peaks extracted from Fig. 1. The other curves give the results of including the contributions of the trajectories 1 and 2 (dot-dashed), 3 and 4 (long-dashed), and 5 and 6 (short-dashed), ordered by the length of their travel times, as well as the coherent sum of all these contributions (solid). Please note that some of these curves almost or completely coincide throughout parts of the spectrum.

energy and for all energies higher than that. For lower energy, however, their contribution becomes insignificant. For  $4.5U_p < E < 6.5U_p$ , again two trajectories dominate the spectrum (long-dashed lines), those with the two next-to-shortest travel times. Finally, in the energy region between  $6.5U_p$  and  $7.5U_p$ , a pair of trajectories with yet longer travel times is the most important one (short-dashed lines). These first six quantum paths having the shortest travel times yield an excellent approximation to the exact spectrum for energies larger than  $4U_p$  except for the two spikes visible at  $E = 5.3U_p$  and  $7.3U_p$ . These spikes always occur at the cutoffs of individual trajectories when one or the other trajectory has to be dropped from the sum (7); cf. Ref. [16]. For energies below  $4U_p$ , the “direct electrons”—those that do not undergo rescattering—become relevant and their trajectories would have to be included.

In Fig. 3 we show a high-harmonic spectrum obtained using the Lewenstein model for the same parameters as in the preceding figures. As before, we compare it to successive approximations in terms of contributions of quantum paths. The same picture results as for HATI: the plateau of linear polarization turns into a staircase, the height of each step is largely identical to the corresponding step in HATI, and the end of each step—its cutoff—is caused by a particular pair of quantum paths.

Both for HHG and for HATI, the solutions of the saddle point equations (4)–(6) are complex. In particular, the start time  $t' \equiv t_0$  and the return time  $t \equiv t_1$  trace out paths (not to be confused with the quantum paths in position space) in the complex plane as a function of harmonic order or electron energy, respectively. These are exhibited in Fig. 4

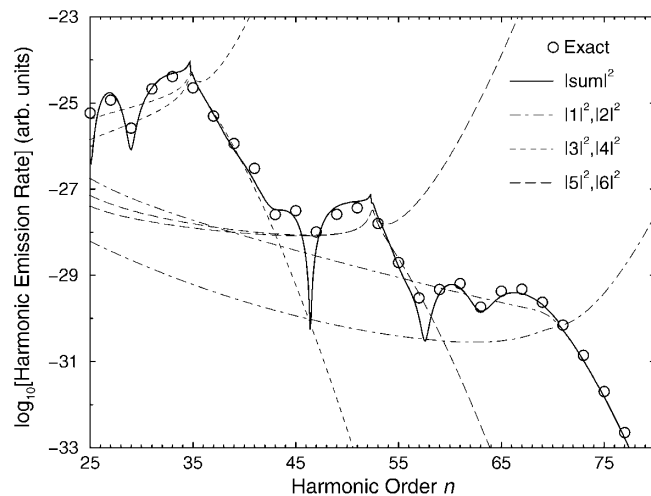


FIG. 3. High-harmonic spectrum for the parameters of Fig. 1 and  $\xi = 0.5$ . The circles are calculated using the Lewenstein model. The various dashed lines are the squared contributions of the quantum paths numbered as in Fig. 2. In contrast to the preceding figure, also the contributions of those trajectories are depicted that have to be dropped after the classical cutoff, causing the spikes. They are characterized by yields that increase exponentially for increasing harmonic order.

for the six trajectories already discussed above. First, we notice that the complex-time orbits for HHG and HATI are very similar. For increasing electron energy or harmonic order the two orbits of a pair first move essentially parallel to the real axis towards some point of closest approach where they appear to repel each other and start parting from each other in the imaginary direction. The point of closest approach corresponds to the cutoff of that pair. This behavior is the same for the start time and for the return time. Notice, however, that the imaginary part of the return time is much smaller than that of the start time.

Finally, in Fig. 5 the real parts of the first six quantum trajectories are depicted for times between  $\text{Re}t'$  and  $\text{Re}t$  for HHG while for HATI the final trajectory of the rescattered electron for times later than  $t$  is displayed, too. The harmonic order and the electron’s energy in each case correspond to comparable positions near the cutoffs of the respective orbits. The trajectories for HHG and for HATI are very similar, underlining again the close relation between the two processes. The trajectories (5,6) with the longest travel times are quite delicate already, going through  $\text{Re}x = 0$  twice before they rescatter. Yet they are

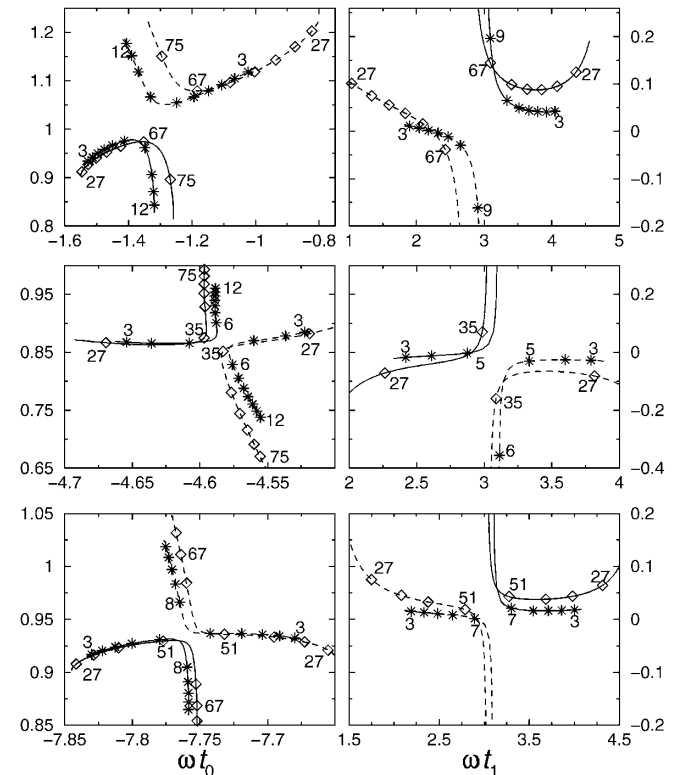


FIG. 4. Paths in the complex plane traced out by the start time  $\omega t_0$  (left-hand panels) and the return time  $\omega t_1$  (right-hand panels) of the six trajectories with the shortest travel times  $\text{Re}\omega(t_1 - t_0)$ . The paths corresponding to HHG are marked with diamonds at intervals of  $\Delta n = 8$ , those for HATI with asterisks at integer multiples of  $U_p$ . For both, the dashed orbits characterize the quantum paths that have to be dropped after the cutoff. The six panels are ordered from top to bottom according to travel time.

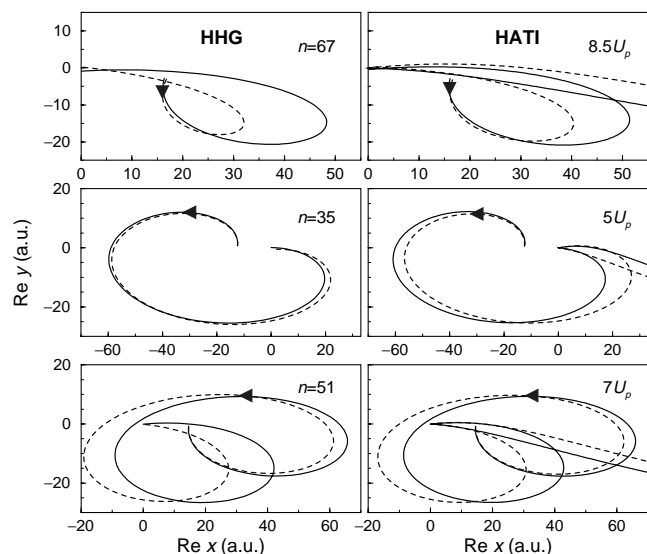


FIG. 5. Real parts of the quantum trajectories that are responsible for three cutoffs of HHG (at  $n = 67, 35,$  and  $51$ ; panels to the left) and HATI (at  $8.5U_p, 5U_p,$  and  $7U_p$ ; panels to the right). The position of the atom is at the origin. The parameters are the same as in Fig. 1 and  $\xi = 0.5$ . As in Fig. 4, the contribution of the dashed trajectory has to be dropped after the cutoff. The arrows mark the direction of the orbits as time goes on.

responsible for a specific part of the spectrum, as discussed above.

The complex quantum paths start from and return to the origin,  $\mathbf{x}(t'_S) = \mathbf{x}(t_S) = 0$ , for the  $n$ th quantum path. In contrast, the orbits plotted in Fig. 5 depart from a position away from the origin by up to 15 a.u., predominantly in the  $x$  direction. This is because we plotted  $\text{Re}\mathbf{x}(t)$  for *real* times  $t \geq \text{Re}t'_S$ , so that the initial condition at the *complex* start time  $t'_S$  is never actually met in the plot; cf. Ref. [16]. Since the return time  $t_S$  is almost real, the orbits closely return to the origin.

It remains to be explained why the plateau characteristic of linear polarization is commuted into a flight of stairs by a field with significant elliptical polarization. This is *not* related to the lengths of the respective travel times. Rather, the clue comes from the fact, visible in Fig. 5, that the trajectories take off essentially in the  $y$  direction, the direction of the small component of the field. A real transverse component  $v_{0y}$  of the initial velocity  $\mathbf{v}_0$  is required in order that the electron return to its starting point. If in Eq. (4) the term  $(mv_{0y})^2$  is moved to the right-hand side, in effect, the binding energy is increased by  $mv_{0y}^2/2$ . A larger binding energy, however, reduces the yield of the process. Extracting a numerical value of  $mv_{0y}$  from the calculated quantum paths shows that indeed this is largest for the orbits (1,2) with the shortest travel times.

Our analysis ignored the Coulomb field during the electron's excursion in the continuum. While *absolute* yields may be substantially enhanced, the *relative* shape of the HHG and HATI spectra appears to be remarkably

independent of the binding potential; cf. Ref. [17] for a comparison to realistic calculations for linear polarization. Moreover, as is evident from Fig. 5, Coulomb effects are less significant for elliptical polarization since typical orbits along their way tend to bypass the ionic core by many atomic units so that "Coulomb refocusing" [18] is less significant than for linear polarization.

In conclusion, we have, for elliptical polarization, performed a detailed analysis of HHG and HATI spectra in terms of quantum paths. Underlining the common origin of the two effects by electrons that revisit the ionic core, both the phenomenology of the plateaus and the quantum paths that generate them are strikingly similar. For high enough ellipticity, the plateau of linear polarization becomes a staircase. Each step can be attributed to a particular pair of quantum paths. In contrast to linear polarization, orbits with comparatively long travel times make important contributions. If means could be devised to affect the orbits in small spatial or temporal regions, this would open the way to wide-ranging manipulation of HHG and ATI spectra.

This work was supported in part by the Deutsche Forschungsgemeinschaft. D.B.M. gratefully acknowledges support from the Alexander von Humboldt Foundation.

\*Also at Faculty of Science and Mathematics, University of Sarajevo, 71000 Sarajevo, Bosnia and Herzegovina.

†Also at Center for Advanced Studies, Department of Physics and Astronomy, University of New Mexico, Albuquerque, NM 87131.

- [1] L. F. DiMauro and P. Agostini, *Adv. At. Mol. Opt. Phys.* **35**, 79 (1995); P. Salières *et al.*, *ibid.* **41**, 83 (1999).
- [2] M. Lewenstein *et al.*, *Phys. Rev. A* **49**, 2117 (1994).
- [3] Ph. Balcou *et al.*, *J. Phys. B* **32**, 2973 (1999).
- [4] M. B. Gaarde *et al.*, *Phys. Rev. A* **59**, 1367 (1999).
- [5] M. Lewenstein *et al.*, *Phys. Rev. A* **51**, 1495 (1995).
- [6] P. B. Corkum, *Phys. Rev. Lett.* **71**, 1994 (1993).
- [7] K. C. Kulander *et al.*, in *Super-Intense Laser-Atom Physics*, NATO ASI, Ser. B, Vol. 316 (Plenum, New York, 1993), p. 95.
- [8] G. G. Paulus *et al.*, *J. Phys. B* **27**, L703 (1994).
- [9] D. B. Milošević and A. F. Starace, *Phys. Rev. Lett.* **81**, 5097 (1998); **82**, 2653 (1999).
- [10] M. Bellini *et al.*, *Phys. Rev. Lett.* **81**, 297 (1998).
- [11] P. Dietrich *et al.*, *Phys. Rev. A* **50**, R3585 (1994).
- [12] B. Gottlieb *et al.*, *Phys. Rev. A* **54**, R1022 (1996).
- [13] K. S. Budil *et al.*, *Phys. Rev. A* **48**, R3437 (1993); Y. Liang *et al.*, *J. Phys. B* **27**, 1269 (1994); N. H. Burnett *et al.*, *Phys. Rev. A* **51**, R3418 (1995); Ph. Antoine *et al.*, *Phys. Rev. A* **53**, 1725 (1996).
- [14] G. G. Paulus *et al.*, *Phys. Rev. Lett.* **80**, 484 (1998).
- [15] A. Lohr *et al.*, *Phys. Rev. A* **55**, R4003 (1997).
- [16] R. Kopold *et al.*, *Opt. Commun.* (to be published).
- [17] R. Kopold and W. Becker, *J. Phys. B* **32**, L419 (1999).
- [18] Th. Brabec *et al.*, *Phys. Rev. A* **54**, R2551 (1996).